



# Trojan strategy assisted phase-pure Fe-NiCo<sub>2</sub>S<sub>4</sub> for industrial anion-exchange membrane water electrolyzer

Fu-Li Wang, Yi-Wen Dong, Cheng-Jie Yu, Bin Dong<sup>\*</sup>, Xin-Yu Zhang, Ruo-Yao Fan, Jing-Yi Xie, Ya-Nan Zhou, Yong-Ming Chai<sup>\*</sup>

State Key Laboratory of Heavy Oil Processing, College of Chemistry and Chemical Engineering, China University of Petroleum (East China), Qingdao 266580, PR China

## ARTICLE INFO

### Keywords:

Phase-pure  
Anion exchange membrane  
Oxygen evolution reaction  
Trojan strategy  
Molten salt

## ABSTRACT

Precise doping into phase-pure structure is very challenging for industrial electrocatalysts keeping high activity and stability. Herein, a facile molten salt method is adopted to synthesize Fe-NiCo<sub>2</sub>S<sub>4</sub> @NIF with a pure phase structure using NiFe foam (NIF) as substrate, achieving controllable Fe doping assisted by inner Fe element in NIF through trojan strategy. Physical characterizations and density functional theory (DFT) calculations reveal that Fe doping not only maintains mechanical strength but also optimizes the electronic structure and reduces \*OOH adsorption energy barrier. Consequently, Fe-NiCo<sub>2</sub>S<sub>4</sub> @NIF only needs a low overpotential of 325 mV to reach the industrial current density of 1000 mA cm<sup>-2</sup> and run stably for 1000 h for oxygen evolution reaction (OER). The anion exchange membrane (AEM) water electrolyzer (Fe-NiCo<sub>2</sub>S<sub>4</sub> @NIF/(Pt/C)) reaches the current density of 1000 mA cm<sup>-2</sup> at a cell voltage of 1.83 V, which operates at the average energy efficiency of 72% for 100 h.

## 1. Introduction

Electrochemical water splitting using renewable energy is a promising route to produce high purity hydrogen for solving the energy crisis and environmental problems [1–3]. In this process, the four-electron oxygen evolution reaction (OER) is the bottleneck with a non-negligible overpotential due to its prolonged kinetic process [4,5]. Therefore, some electrocatalysts are urgently needed to reduce the energy consumption during the OER process for large-scale industrial applications. Currently, the most commercial OER electrocatalysts are Ru- and Ir-based materials. Nevertheless, these precious metal electrocatalysts are scarce and expensive, making them difficult for practical promotion [6–8]. Therefore, the transition metal-based electrocatalysts using earth-abundant elements have been promising alternatives to the noble metal-based electrocatalysts [9,10].

Recently, many inexpensive transition metal-based electrocatalysts have been developed, such as transition-metal phosphides, carbides, oxides, nitride, and hydroxides [11–16]. Compared to transition metal phosphides and carbides, metal sulfides are more tolerant to oxidation atmosphere. While relative to oxides and hydroxides, sulfides play a prominent role in electrocatalysis due to their unique chemical and physical properties, such as high electrical conductivity and mechanical strength. Besides, metal sulfides possess rich redox chemistry, which

contributes to active sites in electrochemical reactions [17,18]. Therefore, many scientists have been attracted to preparing a variety of transition metal sulfides. For example, Yan et al. reported that the mulberry-like NiS/Ni nanoparticles needed the overpotential of 301 mV to reach 10 mA cm<sup>-2</sup>, and the electrode ran 60,000 s at an overpotential of 300 mV [19]. He et al. reported that Ni-BDC@NiS displayed a small overpotential of 330 mV at 20 mA cm<sup>-2</sup> [20]. Although these transition metal sulfides have great activities and stabilities for OER in a lab-scale, it is difficult for these electrocatalysts to exhibit good performance under harsh test conditions (large current density and long-term stability) to achieve industrial demands [17,18]. This is mainly due to the following reasons: (i) these reported metal sulfides by traditional syntheses are challenging to acquire pure phase structure, achieving outstanding conductivity and excellent mechanical strength under industrial conditions. (ii) The current sulfides are evaluated by the three-electrode system in lab-scale, which cannot objectively reveal performance parameters under the industrial operating environment. Therefore, it is urgent to modify the properties of metal sulfide for large-scale hydrogen production.

In order to enhance the performance of sulfide, researchers have employed heteroatomic doping, which can adjust the electronic structure by transferring outer d orbital electrons, optimizing the adsorption energy of the OER intermediate [21,22]. Among the various metal

<sup>\*</sup> Corresponding authors.

E-mail addresses: [dongbin@upc.edu.cn](mailto:dongbin@upc.edu.cn) (B. Dong), [ymchai@upc.edu.cn](mailto:ymchai@upc.edu.cn) (Y.-M. Chai).

sulfides,  $\text{NiCo}_2\text{S}_4$  has attracted special attention since theoretical calculation exhibits its metallic character with extraordinary conductivity compared to semiconductor metal sulfides [23]. The doping of metal elements can increase the number of active sites and speed up electronic transmission, elevating OER activity. Therefore, the design of doped metal sulfides will be an ingenious strategy to improve the electrocatalytic performance. Currently, the design of doped sulfides, including Fe doped NiS and vanadium doped  $\text{NiS}_2$ , have been reported [24,25]. According to statistics, the common doping methods are bulk doping and surface doping, which are difficult to control precisely. Either the doping amount is not enough, and the activity is not significantly modified; or the doping is too much, which is prone to severe lattice distortion, resulting in inferior stability. In addition, the traditional introduction of heteroatoms by additional elements or groups is complicated and time-consuming, limiting its large-scale practical application [26,27]. Therefore, direct synthesizing materials with a high phase-pure and realizing precise and controllable doping is of utmost value but remains highly challenging.

Recently, the molten salt method has been applied to synthesize nanomaterials with uniform composition, excellent crystal morphology, and high phase purity [28,29]. This is mainly because the ion migration rate is accelerated during high temperature liquid molten salt environment, which will promote the mass transfer and nucleation of nanomaterials, synthesizing pure phase structure. The pure-phase structure can promote electron transport and enhance the mechanical strength of the materials, contributing to the conductivity and stability of the electrocatalysts [30,31]. Combining molten salt method with heteroatomic doping, to some extent, seems to be improving the intrinsic activity and stability of the electrocatalyst for practical application. However, the molten salt method is mainly used for the surface treatment of materials and provides a reflection medium for synthesizing nanomaterials [32,33]. The direct synthesis of pure phase nanomaterials by molten salt method and the realization of precise doping is very challenging without a literature report, deserving in-depth study.

For a commercial application, the new generation anion exchange membrane (AEM) electrolyzer attracts much attention because it can use non-precious metal electrocatalysts and evaluate the practical performance of electrocatalysts under the industrial operating environment. Several latest works about AEM electrolyzers also have been reported. For example, Kaczur et al. assembled AEM electrolyzers with  $\text{NiFeCo}$  cathode and  $\text{NiFeO}_x$  anode, reaching  $1 \text{ A cm}^{-2}$  at  $1.90 \text{ V}$  in  $1 \text{ M KOH}$  at  $60^\circ\text{C}$  [34]. Thangavel et al. tested AEM electrolyzers ( $\text{Fe-Ni-Mo-NH}_3/\text{H}_2||\text{NiMo-NH}_3/\text{H}_2$ ) that can achieve  $1 \text{ A cm}^{-2}$  at  $1.57 \text{ V}$  in  $1 \text{ M KOH}$  at  $80^\circ\text{C}$  [35]. However, the synthesis steps of these non-precious metal electrocatalysts are complicated, and the efficiency and practicality need to be further improved. In addition, these AEM electrolyzers are evaluated under high-temperature electrolytes ( $> 50^\circ\text{C}$ ), which limits their large-scale application given the economic costs. Therefore, exploring high-performance electrocatalysts for efficient AEM water electrolysis at room temperature is essential.

In this work, the low-temperature molten salt of KSCN is selected to rapidly synthesize bimetallic sulfides with pure phase structure on the surface of NiFe foam (NIF). At the same time, according to the unique NIF structure of nickel coated iron sandwich framework, we etch the NIF by trojan strategy during molten salt environment so that the internal Fe overflows in a small amount, achieving precise and rapid doping without destroying the original crystal phase structure. The near-pure phase doped electrocatalyst ( $\text{Fe-NiCo}_2\text{S}_4 @\text{NIF}$ ) exhibits excellent activity and stability, which only needs a small overpotential of  $325 \text{ mV}$  at an industrial OER current density of  $1000 \text{ mA cm}^{-2}$  and can maintain  $1000 \text{ h}$  at this current density. Systematic experimental tests and DFT calculations indicate that the introduction of Fe accurately modulates the electronic structure, enhances the electrical conductivity, and optimizes the  $^*\text{OOH}$  adsorption energy to exhibit remarkable OER performance. AEM electrolyzers ( $\text{Fe-NiCo}_2\text{S}_4 @\text{NIF}/(\text{Pt/C})$ ) are constructed by OER electrocatalyst coupled with commercial Pt/C, which achieves

$1000 \text{ mA cm}^{-2}$  at  $1.83 \text{ V}$  and stably operates for  $100 \text{ h}$  maintaining  $72\%$  energy efficiency. Therefore, this paper provides a novel synthesis method of doped transition metal-based OER electrocatalysts with a phase-pure structure to meet the needs of large-scale, low energy consumption, and high stability for AEM water electrolysis.

## 2. Experimental section

The chemicals and materials used in this paper were purchased directly from the enterprise without further purification and processing. The NiFe foam and Ni foam with the same thickness of  $2 \text{ mm}$  was purchased from KunShan JiaYiSheng Electronics CO. LTD.

### 2.1. Synthesis of $\text{Fe-NiCo}_2\text{S}_4 @\text{NIF}$

The  $\text{Fe-NiCo}_2\text{S}_4 @\text{NIF}$  was synthesized for the first time by a novel molten salt method, where the preparation process was shown in Fig. 1. In order to remove oxides and contaminants from the NiFe foam (NIF) surface, the NIF was immersed in hydrochloric acid ( $1 \text{ M HCl}$ ), acetone and ethanol and sonicated for  $20 \text{ min}$ , respectively. Subsequently, the NIF was transferred to a vacuum drying oven at  $60^\circ\text{C}$  overnight. The processed NIF was placed at the bottom of the porcelain boat ( $10 \times 20 \times 3 \text{ mm}$ ) and uniformly covered with the salt mixture of KSCN ( $5 \text{ g}$ ) and  $\text{Co}(\text{NO}_3)_2 \cdot 6 \text{ H}_2\text{O}$  ( $1 \text{ g}$ ). Next, the porcelain boat was put into a muffle furnace and reacted at  $300^\circ\text{C}$  for  $2 \text{ h}$ . After cooling to room temperature, the salt in the porcelain boat becomes blue solid. The final  $\text{Fe-NiCo}_2\text{S}_4 @\text{NIF}$  sample with black color was obtained after rinsing with plenty of DI water and ethanol and dried in a vacuum oven overnight.

### 2.2. Synthesis of $\text{NiCo}_2\text{S}_4 @\text{NF}$

A similar molten salt process synthesized the  $\text{NiCo}_2\text{S}_4 @\text{NF}$ . Firstly, the gray Ni foam (NF) was treated by ultrasound bath for  $20 \text{ min}$  with  $1 \text{ M HCl}$ , acetone and ethanol, respectively. And then, the treated NF was covered with the same proportion of mixture salt ( $5 \text{ g KSCN}$  and  $1 \text{ g Co}(\text{NO}_3)_2 \cdot 6 \text{ H}_2\text{O}$ ) in the porcelain boat and heated at  $300^\circ\text{C}$  for  $2 \text{ h}$ . Finally, the  $\text{NiCo}_2\text{S}_4 @\text{NF}$  sample with black color was washed with water and ethanol several times and dried in a vacuum oven overnight.

### 2.3. AEM water electrolyzer system fabrication

The AEM water electrolyzer (single-cell) was composed of the anode (electrode size of  $1 \text{ cm} \times 1 \text{ cm}$ ), cathode (electrode size of  $1 \text{ cm} \times 1 \text{ cm}$ ), gas diffusion layer (carbon paper), and anion exchange membrane (Fumasep FAA-3-50). We soaked the membrane in KOH for activation treatment  $24 \text{ h}$  prior to use. The active area of the electrolytic cell was  $1 \text{ cm}^2$ .  $\text{Fe-NiCo}_2\text{S}_4 @\text{NIF}$ , NIF and NF were used as anodic electrocatalysts after spraying a certain amount of  $5 \text{ wt\% TP-85}$  (Versogen) ionomer on the top of the electrode. The commercial Pt/C powder was sprayed onto carbon paper as the cathode electrocatalyst. The loading amount of metal Pt is about  $4 \text{ mg cm}^{-2}$ . The electrolyte comprised of  $1 \text{ M KOH}$  ( $25^\circ\text{C}$ ) was recycled from the electrolyte reservoir to the electrolyzer at a stable flow rate of  $40 \text{ ml min}^{-1}$  by a self-priming pump. The AEM electrolyzer was tested using Gamry 3000 with an amplifier, and electrochemical performance was acquired by polarization curves measurements in single-cell from  $1$  to  $2.4 \text{ V}_{\text{cell}}$  at a scan rate of  $5 \text{ mV s}^{-1}$ . The durability was performed at the industrial scale current of  $1000 \text{ mA cm}^{-2}$  to evaluate the AEM water electrolyzer systems. The amount of  $\text{H}_2$  produced from the single cell was measured by a mass flow meter in AEM water electrolyzer testing setup. The following formula calculated the energy efficiency of the electrolyzer.

$$\eta = \frac{E_{\text{Output}}}{E_{\text{Input}}} = \frac{V_{\text{H}_2} \cdot H_0}{W_{\text{H}}} \times 100$$

$W_{\text{H}}$  means the input electricity needed to produce hydrogen,  $H_0$  is the calorific value of hydrogen ( $10.8 \times 10^6 \text{ J m}^{-3}$ , lower heating value), and

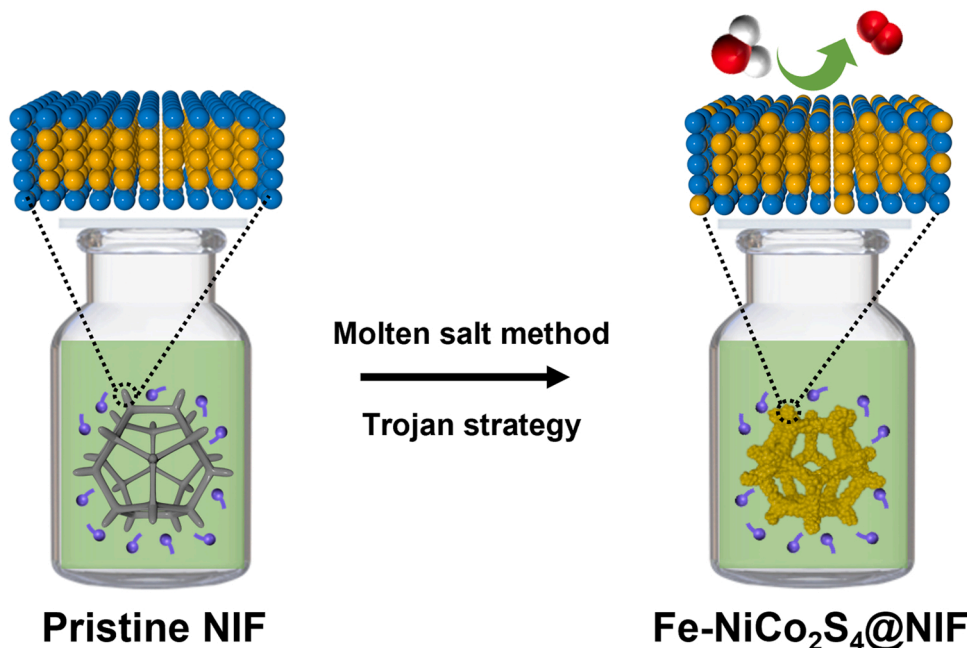


Fig. 1. Schematic illustration of Fe-NiCo<sub>2</sub>S<sub>4</sub> on NiFe foam by a step molten salt method.

the  $V_{H_2}$  represents the total volume of producing hydrogen [36,37].

### 3. Results and discussion

#### 3.1. Electrocatalyst preparation and characterization

As depicted in Fig. 1, the AEM anodic electrode of doped metal sulfide (Fe-NiCo<sub>2</sub>S<sub>4</sub>@NIF) with an almost phase-pure was rapidly synthesized on the surface of NiFe foam (NIF) by molten salt method and Trojan strategy. The unique Fe-NiCo<sub>2</sub>S<sub>4</sub>@NIF nanoparticles can be precisely formed without destroying crystalline phase structure in a bimetallic molten salt environment. NIF and NF have a three-dimensional skeleton structure and smooth surface, which provide

sufficient area support for synthesizing electrocatalysts (Fig. S1). NIF also has a fantastic nickel-coated iron sandwich structure (Fig. S2). When the pristine NIF was placed in the mixed molten salt of KSCN and Co(NO<sub>3</sub>)<sub>2</sub>·6 H<sub>2</sub>O and heated for 2 h, the molten metal salt could be conducive to synthesizing pure-phase metal sulfides by providing the liquid environment with rapid ion migration. At the same time, with the help of the strong polarization during molten salts, trace Fe spilled out from the inside of NIF to achieve atomic precision doping by Trojan strategy. Finally, the bimetallic sulfides precisely regulated by Fe with the pure-phase (Fe-NiCo<sub>2</sub>S<sub>4</sub>@NIF) were synthesized. Furthermore, the catalytic performance was evaluated in the self-assembled AEM water electrolyzer.

The X-ray diffraction (XRD) pattern reveals that the NiCo<sub>2</sub>S<sub>4</sub> (PDF

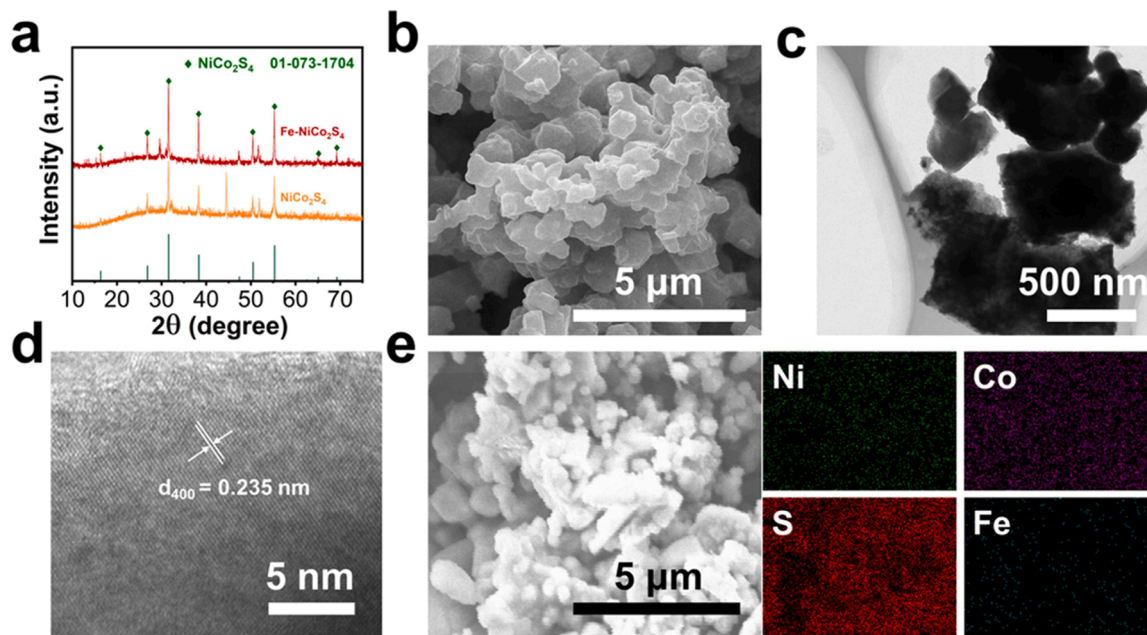


Fig. 2. Characterizations of the Fe-NiCo<sub>2</sub>S<sub>4</sub> nanoparticles on NiFe foam. (a) XRD patterns of Fe-NiCo<sub>2</sub>S<sub>4</sub>@NIF and NiCo<sub>2</sub>S<sub>4</sub>@NF. (b) SEM, (c) TEM, (d) HRTEM images and (e) EDS elemental mapping images of Ni, Co, S and Fe of Fe-NiCo<sub>2</sub>S<sub>4</sub>@NIF.



No. 01–073–1704) with approximate pure phase is successfully synthesized. The diffraction peaks at  $2\theta$  values of 16.3, 26.8, 31.6, 38.3, 47.4, 50.5 and 55.3° (Fig. 2a), which can be indexed to (111), (220), (311), (400), (422), (511) and (440), respectively [38]. Moreover, the XRD diffraction peak does not shift after doping Fe. This phenomenon fully illustrates that the trojan strategy with unique advantages could contribute to achieving atomic-level doping without destroying the lattice structure. The scanning electron microscopy (SEM) reveals that the intertwined nanoparticles (Fe-NiCo<sub>2</sub>S<sub>4</sub> @NIF) have a thickness of ~500 nm and that they have grown on the NIF surface (Fig. 2b and Fig. S3). By contrast, NiCo<sub>2</sub>S<sub>4</sub> @NF is a stack of nanosheets with a thickness of ~25 nm (Fig. S4). The porous structure of Fe-NiCo<sub>2</sub>S<sub>4</sub> @NIF (Fig. 2c and Fig. S5) can be observed at the edge of nanoparticles by Transmission electron microscopy (TEM), which may be due to the etching effect of the strongly polar molten salt environment and will be beneficial to facilitate mass transportation in the reactions [28,39]. Then, the sample of Fe-NiCo<sub>2</sub>S<sub>4</sub> @NIF is characterized by nitrogen absorption/desorption isotherm to confirm the existence of porous structure. The nitrogen absorption/desorption isotherm of Fe-NiCo<sub>2</sub>S<sub>4</sub> @NIF (Fig. S6) reveals a Brunauer-Emmett-Teller (BET) surface area of 17.71 m<sup>2</sup> g<sup>-1</sup>. And Barrett-Joyner-Halenda (BJH) pore-size distribution implies that Fe-NiCo<sub>2</sub>S<sub>4</sub> @NIF has the mesoporous structures with average pore diameter of 4.39 nm. The high-resolution TEM (HRTEM) image (Fig. 2d) reveals good crystallinity with clear lattice fringes, exhibiting that the structure of the high crystal phase is still maintained after precise doping. The HRTEM image displays lattice spacings of 0.235 nm, which is associated with the (400) crystallographic planes of NiCo<sub>2</sub>S<sub>4</sub> and agrees with the XRD patterns. The energy dispersive spectroscopy (EDS) elemental mapping images (Fig. 2e) clarify the coexistence of Ni, Co, S and Fe in Fe-NiCo<sub>2</sub>S<sub>4</sub> @NIF. The EDS analysis (Fig. S7) indicates that the atomic ratio of Fe, Ni, Co and S in the nanoparticles corresponds to a Fe<sub>0.035</sub>NiCo<sub>2.02</sub>S<sub>3.16</sub> stoichiometry. Although there may be some aberration in the EDS, its results are in good agreement with XRD measurements and confirm the successful preparation of precisely doped bimetallic sulfides (Fe-NiCo<sub>2</sub>S<sub>4</sub> @NIF).

X-ray photoelectron spectroscopy (XPS) is applied to obtain information about the surface composition and chemical states of the prepared electrocatalysts. Fig. 3a reveals the survey spectra of Fe-NiCo<sub>2</sub>S<sub>4</sub> @NIF and NiCo<sub>2</sub>S<sub>4</sub> @NF, where the Fe element is present in the Fe-NiCo<sub>2</sub>S<sub>4</sub> @NIF electrocatalyst showing a consistent trend with EDS. The high-resolution Ni 2p spectrum of Fe-NiCo<sub>2</sub>S<sub>4</sub> @NIF exhibits two peaks of spin-orbit doublets corresponding to Ni<sup>3+</sup> and Ni<sup>2+</sup>, including Ni<sup>3+</sup> located at 856.2 and 874.7 eV, and Ni<sup>2+</sup> at 855.2 and 872.7 eV (Fig. 3b). Two related satellite peaks and metallic Ni peak located at 879.4, 860.8 and 852.4 eV are observed, respectively. The Ni 2p<sub>3/2</sub> and Ni 2p<sub>1/2</sub> binding energy of Fe-NiCo<sub>2</sub>S<sub>4</sub> @NIF are about 0.3 eV larger than that of NiCo<sub>2</sub>S<sub>4</sub> @NF. And the content of Ni<sup>3+</sup> is higher in Fe-NiCo<sub>2</sub>S<sub>4</sub> @NIF compared with NiCo<sub>2</sub>S<sub>4</sub> @NF. The phenomenon of Ni peak change is mainly attributed to the altered electronic structure after doping Fe [40, 41]. The fitted peaks at 780.7 eV for Co 2p<sub>3/2</sub> and 796.3 eV for Co 2p<sub>1/2</sub> are spin-orbit characteristics of Co<sup>2+</sup>, while those peaks situated at 777.9 eV for Co 2p<sub>3/2</sub> and 792.8 eV for Co 2p<sub>1/2</sub> are spin-orbit characteristics of Co<sup>3+</sup> (Fig. 3c). These peaks of Fe-NiCo<sub>2</sub>S<sub>4</sub> @NIF move towards the lower binding energy compared with NiCo<sub>2</sub>S<sub>4</sub> @NF, indicating that the introducing of Fe also has a strong electronic interaction on Co atoms [42]. In the Fe 2p region of Fe-NiCo<sub>2</sub>S<sub>4</sub> @NIF (Fig. 3d), the peaks at 713.2 and 726.4 eV can be assigned to Fe<sup>3+</sup>, accompanied by a satellite peak at 726.5 eV. The binding energies at 710.5 and 723.9 eV correspond to Fe<sup>2+</sup>, containing a satellite peak at 719.2 eV. Except for those peaks, the peak at 708.2 eV is observed to be consistent with Fe-S, further demonstrating the successful doping of Fe in the electrocatalyst [43,44]. The S 2p spectrum (Fig. 3e) of Fe-NiCo<sub>2</sub>S<sub>4</sub> @NIF displays that these peaks at 160.9 and 163.1 eV could be well-fitted with 2p<sub>3/2</sub> and 2p<sub>1/2</sub>, detailedly assigned to S<sup>2-</sup> and the metal-sulfur bond. The signal of the S-O bands located at 168.3 eV is derived from the solvent or oxidized S [40,45]. The binding energy of S 2p for Fe-NiCo<sub>2</sub>S<sub>4</sub> @NIF displays the negative shift of 0.4 eV compared with that of pristine NiCo<sub>2</sub>S<sub>4</sub> @NF, which might be caused by the electronic delocalization from the outer orbitals of Fe atoms towards S atoms [46]. Moreover, the O 1s XPS spectra of Fe-NiCo<sub>2</sub>S<sub>4</sub> @NIF in Fig. 3f proves

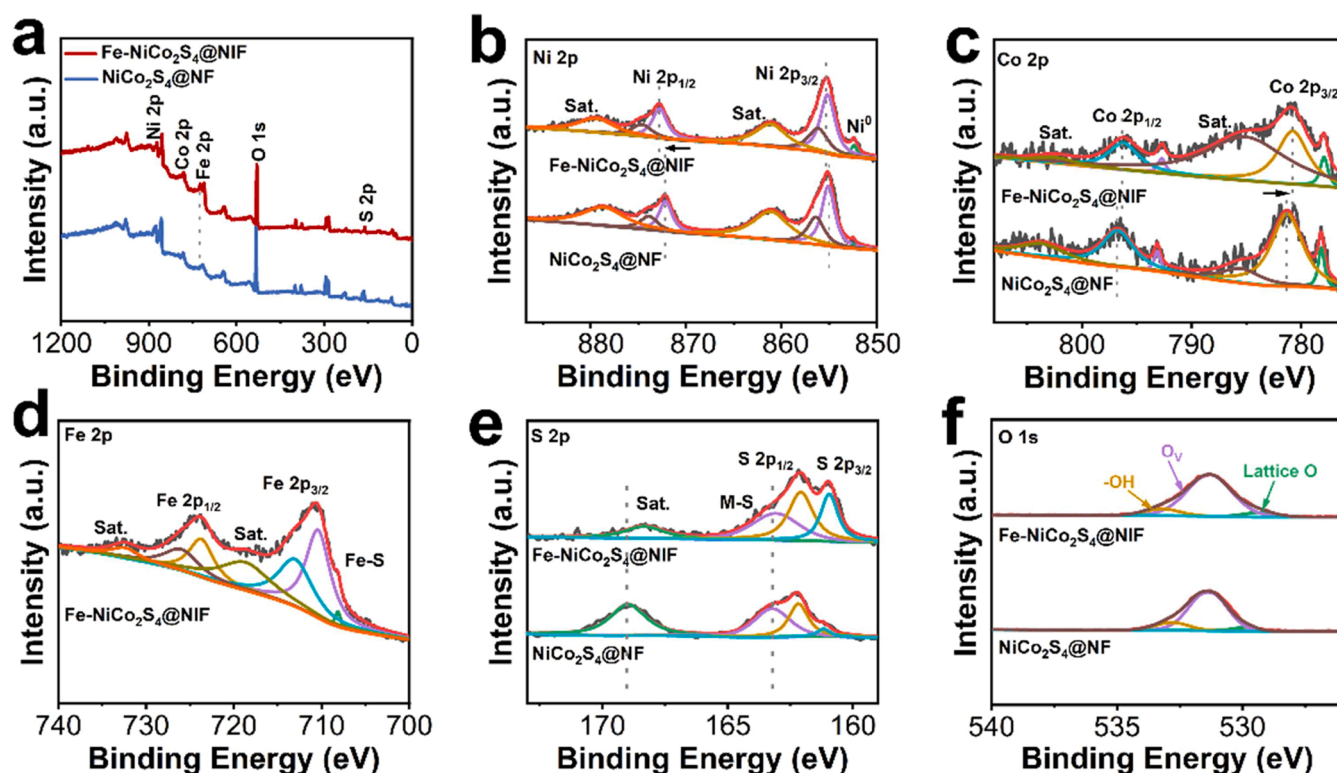


Fig. 3. XPS spectra of (a) survey, (b) Ni 2p, (c) Co 2p, (d) Fe 2p, (e) S 2p and (f) O 1s for Fe-NiCo<sub>2</sub>S<sub>4</sub> @NIF and NiCo<sub>2</sub>S<sub>4</sub> @NF.

three different peaks at 529.5, 531.3, and 533.2 eV, which can be attributed to lattice oxygen (Lattice O), oxygen vacancies ( $O_v$ ) and -OH groups (M-OH), respectively [47–49]. The content of oxygen vacancies increased from 63% to 66% after doping Fe, revealing that the Fe-Ni-Co<sub>2</sub>S<sub>4</sub>@NIF has more amount of oxygen vacancies compared with pure NiCo<sub>2</sub>S<sub>4</sub>@NF. The generation of oxygen vacancies could drastically regulate the surface electronic state of the active sites and optimize the adsorption energies of the reaction intermediates, leading to promoted charge transfer rates and boosted intrinsic activity. Furthermore, the vacancies with an unsaturated coordination structure render abundant active sites and further improve the reactivity [50,51]. And the peak of 664.6 cm<sup>-1</sup> for NiCo<sub>2</sub>S<sub>4</sub>@NF shifts to 670.5 cm<sup>-1</sup> for Fe-NiCo<sub>2</sub>S<sub>4</sub>@NF (Fig. S8), further explaining the accurate introduction of trace Fe extensively regulates the electronic structure among atoms in the electrocatalyst and promotes electron transfer [40].

### 3.2. Electrocatalytic activities

Firstly, we investigate the electrochemical OER performance of the Fe-NiCo<sub>2</sub>S<sub>4</sub>@NIF electrode and other comparative samples. Fig. 4a exhibits LSV polarization curves for different electrodes, including Fe-

NiCo<sub>2</sub>S<sub>4</sub>@NIF, NiCo<sub>2</sub>S<sub>4</sub>@NF, NIF and NF with a scan rate of 1.0 mV s<sup>-1</sup> in 1 M KOH solutions. The oxidation peak of nickel species in the Fe-NiCo<sub>2</sub>S<sub>4</sub>@NIF is greatly suppressed compared with that of NiCo<sub>2</sub>S<sub>4</sub>@NF. The phenomenon is mainly because the accurate Fe doping regulates the electronic structure of Ni atoms and increases the content of high valence Ni<sup>3+</sup>, which also corresponds to the results of XPS analysis [52–54]. And Fe-NiCo<sub>2</sub>S<sub>4</sub>@NIF, with the best OER performance, only requires a lower overpotential of 307 and 327 mV to drive the large current density of 500 and 1000 mA cm<sup>-2</sup> (Fig. 4b), which is better than those of NiCo<sub>2</sub>S<sub>4</sub>@NF (366 mV for 500 mA cm<sup>-2</sup> and 411 mV for 1000 mA cm<sup>-2</sup>), NIF (454 mV for 500 mA cm<sup>-2</sup> and 500 mV for 1000 mA cm<sup>-2</sup>) and NF (754 mV for 500 mA cm<sup>-2</sup> and 800 mV for 1000 mA cm<sup>-2</sup>). As depicted in Fig. 4c, the Tafel slope for the Fe-NiCo<sub>2</sub>S<sub>4</sub>@NIF electrode is 58.8 mV dec<sup>-1</sup>, which is much smaller than that of the NiCo<sub>2</sub>S<sub>4</sub>@NF electrode (116.1 mV dec<sup>-1</sup>), NIF electrode (137.1 mV dec<sup>-1</sup>), and the NF electrode (187.3 mV dec<sup>-1</sup>), indicating that the introduction of Fe greatly accelerates the kinetics of OER reaction. In addition, the electrochemical double layer capacitances ( $C_{dl}$ ) with a linear relationship to electrochemically active surface area (ECSA) are investigated further to explain the improvement of electrocatalyst performance [55,56]. The CV test could obtain  $C_{dl}$  at various

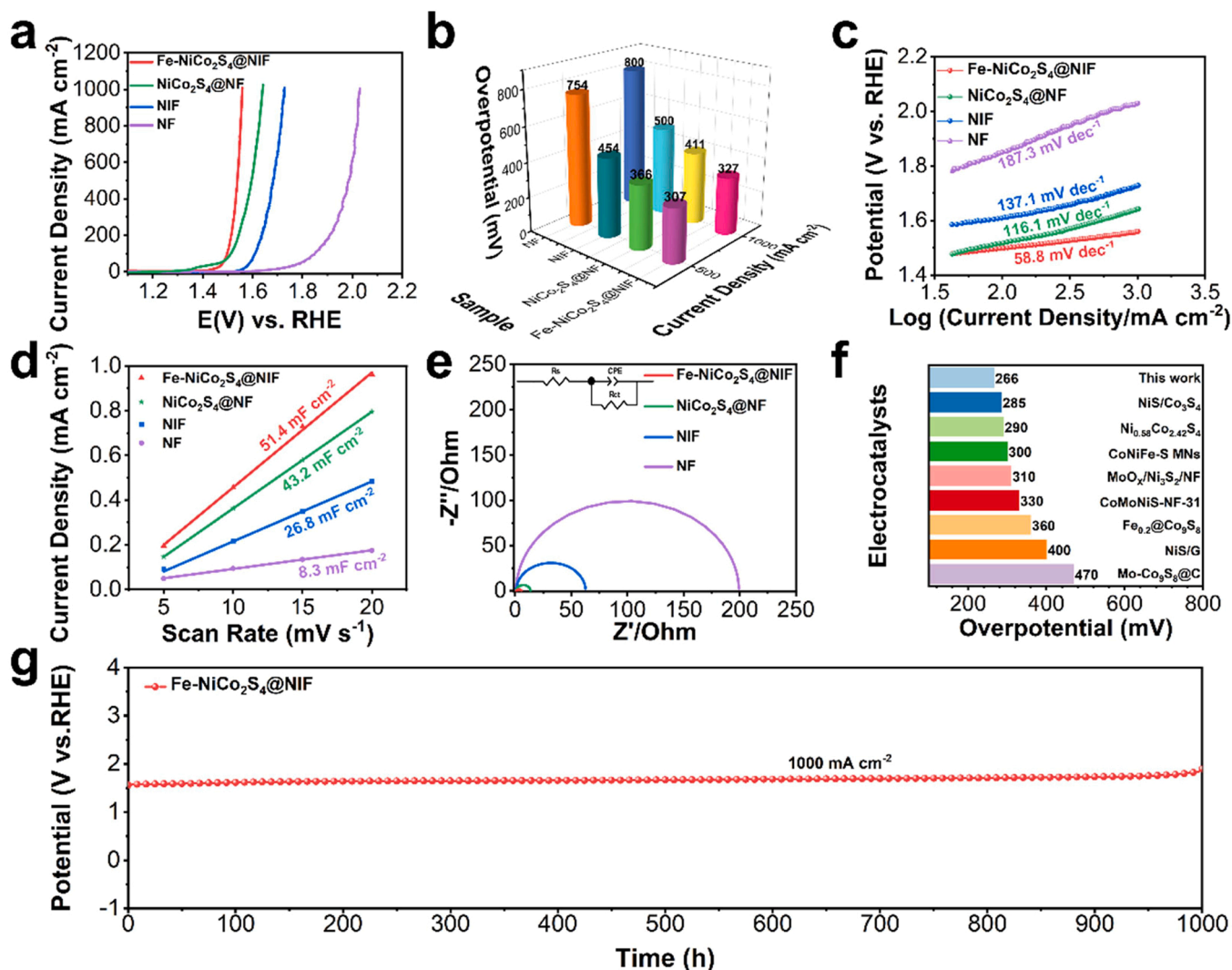


**Fig. 4.** (a) OER polarization curves of Fe-NiCo<sub>2</sub>S<sub>4</sub>@NIF, NiCo<sub>2</sub>S<sub>4</sub>@NF, NIF and NF in 1 M KOH solution. (b) Corresponding the OER overpotentials at 500 and 1000 mA cm<sup>-2</sup>. (c) Tafel slopes of Fe-NiCo<sub>2</sub>S<sub>4</sub>@NIF, NiCo<sub>2</sub>S<sub>4</sub>@NF, NIF and NF for OER. (d) Double layer capacitor of the as-prepared electrocatalysts. (e) Electrochemical impedance spectra (EIS) of Fe-NiCo<sub>2</sub>S<sub>4</sub>@NIF, NiCo<sub>2</sub>S<sub>4</sub>@NF, NIF and NF. (f) Comparison of the overpotentials to achieve the OER current density of 100 mA cm<sup>-2</sup> for Fe-NiCo<sub>2</sub>S<sub>4</sub>@NIF with reported electrocatalysts. References are listed in Supporting Information. (g) Chronopotentiometry curves of the Fe-NiCo<sub>2</sub>S<sub>4</sub>@NIF in 1 M KOH at a current density of 1000 mA cm<sup>-2</sup> for 1000 h.

scanning rates in a non-Faradaic potential range (Fig. S9). Fig. 4d exhibits that the  $C_{dl}$  of Fe-NiCo<sub>2</sub>S<sub>4</sub> @NIF, NiCo<sub>2</sub>S<sub>4</sub> @NF, NIF and NF are 51.4, 43.2, 26.8 and 8.3 mF cm<sup>-2</sup>, and the corresponding ECSAs are calculated to be 1285, 1080, 670 and 207.5 cm<sup>2</sup>, respectively. After the ECSA normalization of LSV curves, as can be seen in Fig. S10, the Fe-NiCo<sub>2</sub>S<sub>4</sub> @NIF still has lower overpotential than those of NiCo<sub>2</sub>S<sub>4</sub> @NF, NIF and NF, which further demonstrates the enhancement of intrinsic activity is attributed to the decoration of Fe with abundant active sites. To eliminate the interference of the substrate, the geometric activity and specific activity per BET surface area are shown in Fig. S11. Noted that the Fe-NiCo<sub>2</sub>S<sub>4</sub> @NIF operated with the highest specific current densities per geometric surface area and BET surface area for OER, further suggesting the superior catalytic activities of the Fe-NiCo<sub>2</sub>S<sub>4</sub> @NIF. In order to better demonstrate the charge transfer efficiency, electrochemical impedance spectroscopy (EIS) is performed to study the conductivity of the electrode towards OER [57]. As revealed in Fig. 4e, Fe-NiCo<sub>2</sub>S<sub>4</sub> @NIF delivers a much lower charge-transfer resistance ( $R_{ct}$ , 4.5  $\Omega$ ) than NiCo<sub>2</sub>S<sub>4</sub> @NF (12.7  $\Omega$ ), NIF (61.8  $\Omega$ ), and NF (198.3  $\Omega$ ), demonstrating that the Fe-NiCo<sub>2</sub>S<sub>4</sub> @NIF possesses the lower impedance and most competent charge transfer kinetics corresponding to the Tafel results. This further suggests that the doped electrocatalysts keeping an entire pure phase have outstanding advantages in conductivity. It can be noted that the OER performance of Fe-NiCo<sub>2</sub>S<sub>4</sub> @NIF has exceeded most of the previously reported transition metal-based sulfides, especially at industrial-scale large current densities with extremely excellent performance (Fig. 4f and Table S1).

From the view of practical application, the long-time stability under the large current density is a necessary evaluation for electrocatalysts [58,59]. Therefore, we have designed a device for simulating industrial stability operation under laboratory conditions (Fig. S12). By using the device to replenish water automatically, the problem caused by a drastic change of electrolyte concentration under a large current density can be solved to maintain a relatively steady process. Ultra-long chronopotentiometry test (Fig. 4g) indicates that the Fe-NiCo<sub>2</sub>S<sub>4</sub> @NIF can run stably for 1000 h at 1000 mA cm<sup>-2</sup> without noticeable performance degradation, exhibiting extraordinary stability and promising industrial application prospects. The superb stability of Fe-NiCo<sub>2</sub>S<sub>4</sub> @NIF could be mainly ascribed to the unique structure by the molten salt method, in which the NiCo<sub>2</sub>S<sub>4</sub> with a determined phase-pure structure will greatly enhance the conductivity and stability. Moreover, the Fe atoms endlessly spilled through the trojan strategy can accurately regulate the electronic structure and provide plentiful active sites to maintain the ultra-long activity and stability. The Faraday efficiency (FE) of the sample was evaluated by comparing the calculated and experimental gas yields. As shown in Fig. S13, the amount of H<sub>2</sub> or O<sub>2</sub> theoretically calculated agrees well with the experimentally measured value of Fe-NiCo<sub>2</sub>S<sub>4</sub> @NIF at the current density of 100 mA cm<sup>-2</sup>, representing a nearly 100% FE for HER or OER. The electrocatalyst Fe-NiCo<sub>2</sub>S<sub>4</sub> @NIF, after a long-time stability test, is further characterized by SEM, EDS-mappings and XPS to verify the splendid mechanical strength. SEM images (Fig. S14) with different magnifications reveal that the nanoparticles still remain on the surface of the NIF after the stability test. Some nanosheets around the nanoparticles may be due to the in-situ surface reconstruction of metal hydroxides during the long-time OER testing in alkaline electrolytes [18]. Compared with the original Fe-NiCo<sub>2</sub>S<sub>4</sub> @NIF, the EDS-mappings show that the S and Fe have marked changes (Fig. S15). The content of S is significantly reduced after the OER test in a three-electrode system, which also confirms the in-situ conversion process of sulfide into hydroxide in agreement with the SEM results, seeming to have a positive effect on the wonderful stability [60]. The content of the Fe element increases, which may be due to Fe spillover from NIF during a long-time stability testing. The XPS peaks of Fe, Ni, Co, S and O are still reserved in Fig. S16a after the OER test. And the peaks of Fe, Co, Ni, and S at low valence disappeared or weakened. The fitting data of Ni 2p in Fig. S16b illustrates that the proportion of Ni (III) is higher than that of Ni (II), which should be due to the generation

of more active Ni<sup>3+</sup> in NiOOH species. As depicted in Fig. S16c, d, Co<sup>2+</sup> and Fe<sup>2+</sup> are wholly oxidized to Co<sup>3+</sup> and Fe<sup>3+</sup> by the amount of oxygen because of their strong reducibility to Ni. For S 2p (Fig. S16e), the signal strength weakens significantly, which may be due to the conversion from metal sulfide to hydroxide. Specially, the peak percentage of M-O/OOH in O 1s (Fig. S16f) increases from 26.5% to 34.4% compared with before the OER test, further confirming the formation of metal hydroxide [61].

### 3.3. Lab-scaled AEMWE single-cell testing

To evaluate the industrial-scale hydrogen production ability of the electrocatalyst, we assemble a single cell AEM water electrolyzer by coupling Fe-NiCo<sub>2</sub>S<sub>4</sub> @NIF anode electrocatalyst and commercial Pt/C cathode electrocatalyst (Fe-NiCo<sub>2</sub>S<sub>4</sub> @NIF/(Pt/C)) and compared its performance with that of an AEM water electrolyzer prepared by pairing (Pt/C) cathode with the NIF (NIF/(Pt/C)) and NF (NF/(Pt/C)) (Fig. 5a-c). Fig. 5d shows the polarization curves at room temperature (25 °C) in 1 M KOH with iR compensation. The performance of the Fe-NiCo<sub>2</sub>S<sub>4</sub> @NIF/(Pt/C) based on the AEM water electrolyzer far exceeds that of NIF/(Pt/C) and NF/(Pt/C). NIF/(Pt/C) and NF/(Pt/C) electrolyzer require a high cell voltage of 2.08 and 2.21 V to reach 1000 mA cm<sup>-2</sup>, respectively. In contrast, our AEM electrolyzer (Fe-NiCo<sub>2</sub>S<sub>4</sub> @NIF/(Pt/C)) only obtains the lower cell voltage of 1.83 V to achieve the same current density (1000 mA cm<sup>-2</sup>). And the electrolyzer (Fe-NiCo<sub>2</sub>S<sub>4</sub> @NIF/(Pt/C)) exhibits extraordinary current density under different cell voltages (Fig. 5e). Even more surprising, the performance of our AEM electrolyzer (Fe-NiCo<sub>2</sub>S<sub>4</sub> @NIF/(Pt/C)) also outperforms most single-cell AEM electrolytic cells reported to date under low temperature operating conditions (Fig. 5f and Table S2). The excellent property of the electrolyzer should be attributed to using a pure-phase anodic electrocatalyst (Fe-NiCo<sub>2</sub>S<sub>4</sub>) with abundant active sites synthesized by the molten salt method and trojan strategy. Then, we run the AEM electrolyzer (Fe-NiCo<sub>2</sub>S<sub>4</sub> @NIF/(Pt/C)) at a constant current density of 1000 mA cm<sup>-2</sup> to investigate the efficiency of hydrogen production and the stability of the electrocatalyst under realistic operating conditions. Fig. 5g illustrates that the electrolyzer can keep the current density of 1000 mA cm<sup>-2</sup> running stably for 100 h under the cell voltage of 1.83 V, exhibiting better stability than most AEM cells in recent literature. Furthermore, the amount of H<sub>2</sub> produced from the single cell is about 7.5 ml min<sup>-1</sup> by amass flow meter, and the average energy efficiency is higher than 72% during the 100-h test (Fig. S17). The above results demonstrate that the Fe-NiCo<sub>2</sub>S<sub>4</sub> @NIF with a unique crystal structure is a highly active electrocatalyst for OER and AEM, which can be used for large-scale and efficient hydrogen production with a broad industrial prospect.

### 3.4. Theoretical calculation

Density functional theory (DFT) calculations are carried out to explain the OER mechanism of the synthesized electrocatalysts and to reveal the positive effect of Fe doping. Firstly, NiCo<sub>2</sub>S<sub>4</sub> bulk model is selected as calculated structure. The simulated XRD pattern (Fig. S18) is in agreement with the XRD of experimental test, confirming the bulk model with theoretically reliable structure. Moreover, the (111), (110), (100) and (220) facets are selected to calculate surface energy (Table S3). The (220) facet with the lowest surface energy is determined to be the thermodynamically most stable surface. In order to determine the reasonable doping site, the formation energy for different replaced sites is calculated. Table S4 shows the formation energy of the Ni and Co sites. It is observed that the replacement of the Fe at Co site has the smaller formation energy compared with Ni site, confirming that Fe atom is thermodynamically stable doping at Co site [62]. According to the XRD and DFT results, the NiCo<sub>2</sub>S<sub>4</sub> (220) facets are selected as active surfaces for the calculation model. The ideal electron step requires 1.23 eV in the OER process, but the practical energy is higher than



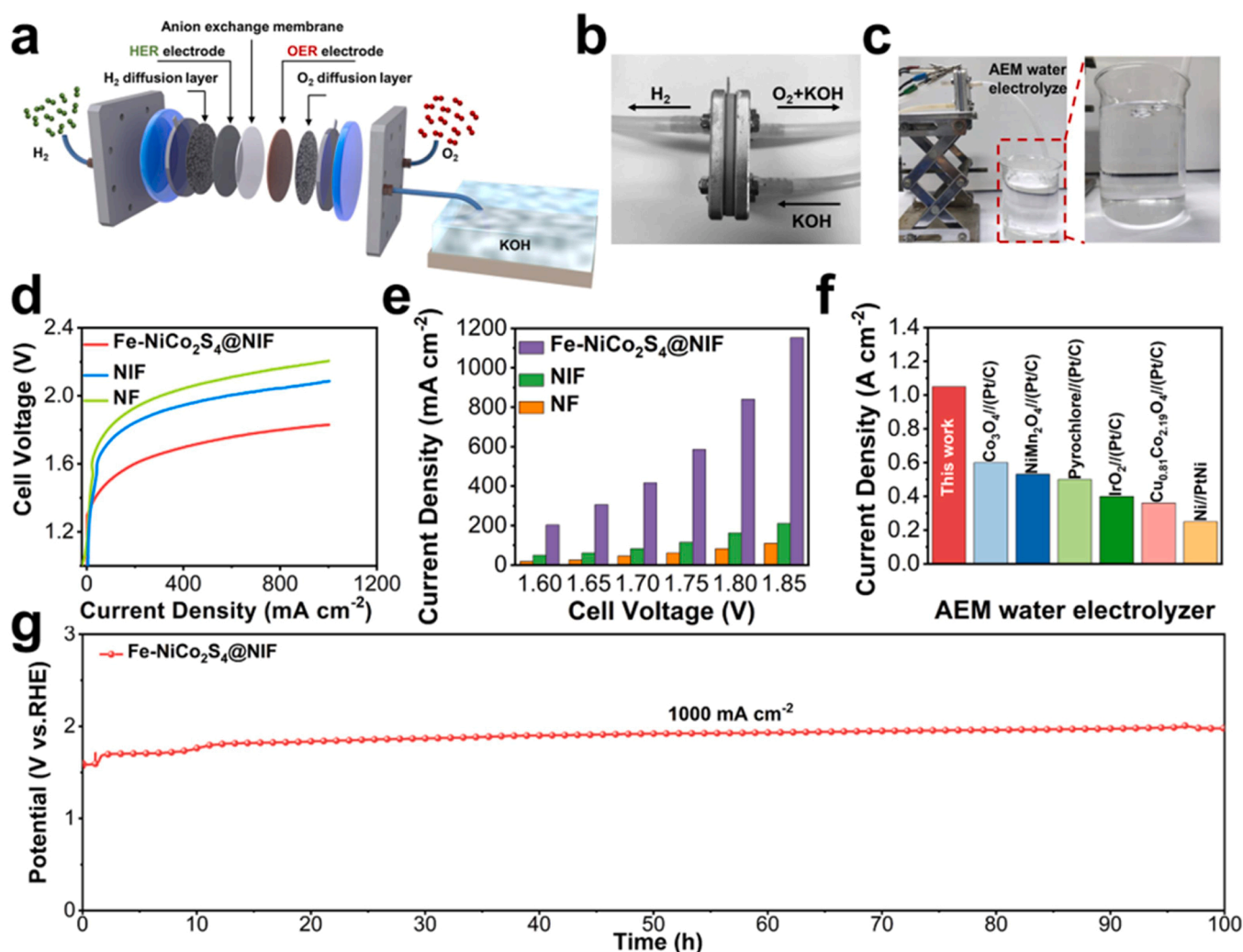


**Fig. 5.** (a) Schematic illustration of the designed AEM water electrolyzer. Photographs of (b) AEM water electrolyzer and (c) evolved hydrogen. (d) Polarization curves of AEM water electrolyzer for Fe-NiCo<sub>2</sub>S<sub>4</sub>@NIF/(Pt/C), NIF/(Pt/C), and NF/(Pt/C) cells recorded at 25 °C in 1 M KOH solution. (e) Current density at various cell voltages for Fe-NiCo<sub>2</sub>S<sub>4</sub>@NIF/(Pt/C), NIF/(Pt/C), and NF/(Pt/C) cells. (f) Comparison the current density of AEM water electrolyzer for the Fe-NiCo<sub>2</sub>S<sub>4</sub>@NIF/(Pt/C) cell and the reported AEM water electrolyzer cells at the cell voltage of about 1.8 V. (g) Durability cell voltage-time plots for the AEM water electrolyzer at a constant current density of 1000 mA cm<sup>-2</sup> for 100 h.

1.23 eV due to the overpotential. Therefore, we first calculate the free energy of Fe-NiCo<sub>2</sub>S<sub>4</sub>@NIF and NiCo<sub>2</sub>S<sub>4</sub>@NF to obtain the theoretical overpotential by the potential determining step (PDS).

Optimized computational structural models with different sites and intermediates are displayed in Fig. S19–S22. Fig. 6a illustrates the OER process on Fe-NiCo<sub>2</sub>S<sub>4</sub>@NIF with the Fe atom regarded as the active site. The Gibbs free energy of each step for different sites in Fe-NiCo<sub>2</sub>S<sub>4</sub>@NIF and NiCo<sub>2</sub>S<sub>4</sub>@NF at the potential of 0 V are calculated and displayed in Fig. S23a and Table S5. The calculated potential gaps (Fig. S23b) of the RDS during the OER process for the Fe, Co and Ni sites in Fe-NiCo<sub>2</sub>S<sub>4</sub>@NIF are 1.50, 1.52 and 2.75 eV, respectively, revealing that Fe is regarded as the active site. Moreover, the OER process for NiCo<sub>2</sub>S<sub>4</sub>@NF is also calculated, for which the Co site obtains a lower RDS (1.56 eV), considering as the active center. When the oxidation potential is 1.23 V (Fig. 6b), the needed ΔG from O\* to OOH\* is 0.33 eV (NiCo<sub>2</sub>S<sub>4</sub>@NF), and the theoretical overpotential is 0.33 V. While the overpotential for Fe-NiCo<sub>2</sub>S<sub>4</sub>@NIF is only 0.27 V. The theoretical overpotential decreases by 60 mV after introduction of Fe. The above results reveal that Fe-NiCo<sub>2</sub>S<sub>4</sub>@NIF has more favorable OER kinetics than NiCo<sub>2</sub>S<sub>4</sub>@NF, which corresponds to the results of Tafel and EIS in the electrochemical section. Moreover, the d-band center can describe the bonding strength between the OER intermediates and the adsorption

surface, reflecting the electrical conductivity of the material [63]. The partial density of states (PDOS) of Fe-NiCo<sub>2</sub>S<sub>4</sub>@NIF and NiCo<sub>2</sub>S<sub>4</sub>@NF is analyzed using the optimal configuration shown in Fig. 6c, d. The PDOS diagram in Fig. 6e displays that these materials have metallic properties as Fermi energies lie within the band, revealing the advantages of pure-phase sulfides in intrinsic conductivity by the molten salt method. Replacement of Fe at the Co site results in a higher DOS near the Fermi level, which will improve the electrical conductivity of the materials and be in consistent with EIS results [46]. In addition, the calculated PDOS reveals that the d-band center shifts toward the Fermi level after Fe doping (from −1.15 to −1.06 eV), suggesting a robust chemical bonding ability to OER intermediates, which can help to reduce the energy barrier of the reaction and promote the release of oxygen. The computed Bader charges reveal that doping with relatively less electronegative Fe at a Co site increases the electron densities of the neighboring S atoms as their net charges become more negative (Fig. S24). And this phenomenon is consistent with the results of XPS analysis [23]. This charge transfer process will be beneficial to enhancing the overall conductivity of the electrocatalyst and optimizing the adsorption energy for intermediates, achieving splendid OER performance.

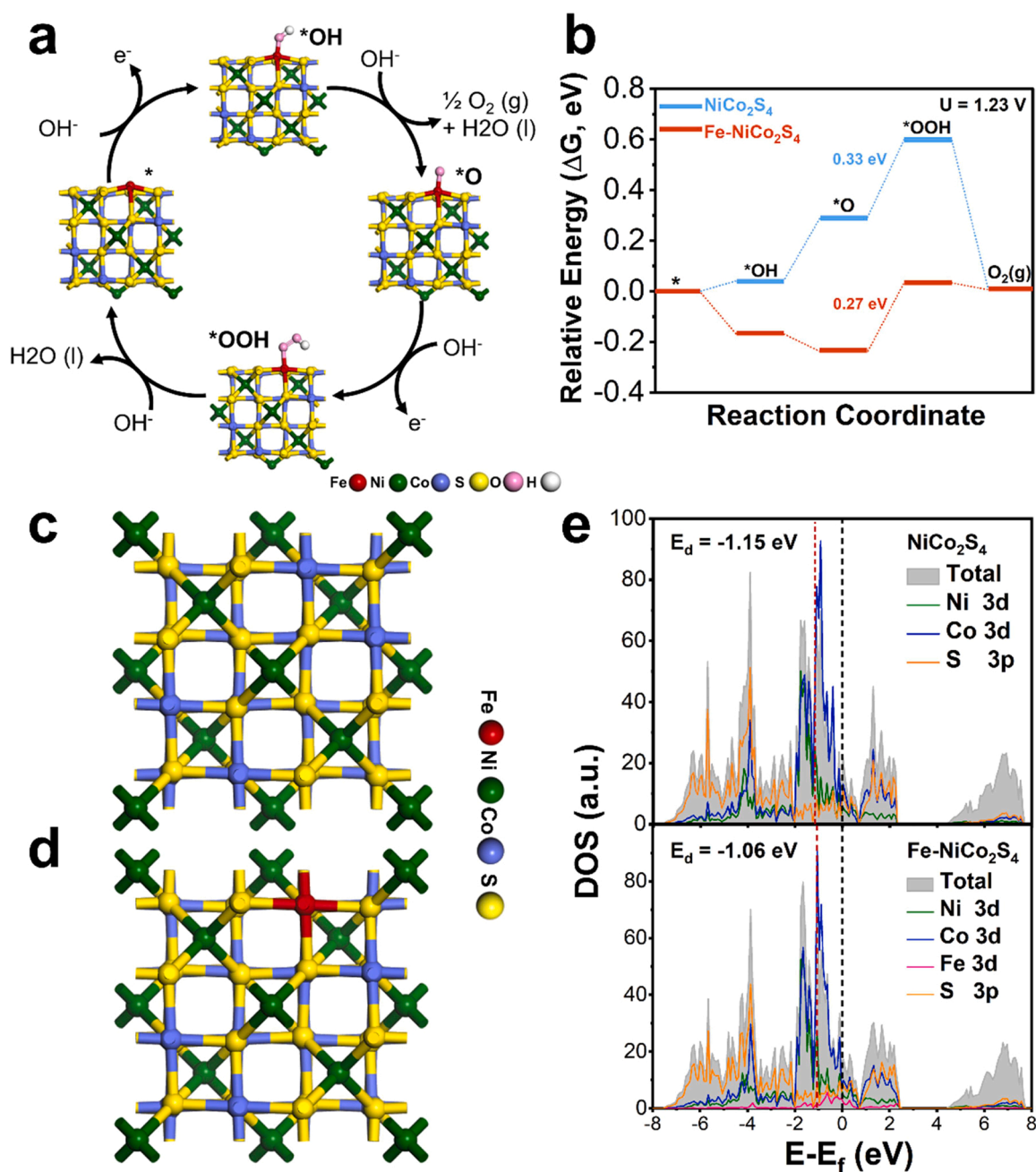


**Fig. 6.** (a) Alkaline OER mechanism on Fe-NiCo<sub>2</sub>S<sub>4</sub> @NIF for DFT calculation. (b) Gibbs free-energy diagram for the four OER steps on Fe-NiCo<sub>2</sub>S<sub>4</sub> @NIF and NiCo<sub>2</sub>S<sub>4</sub> @NF. Optimized crystal structure of (c) NiCo<sub>2</sub>S<sub>4</sub> @NF and (d) Fe-NiCo<sub>2</sub>S<sub>4</sub> @NIF. (e) Calculated PDOS for Fe-NiCo<sub>2</sub>S<sub>4</sub> @NIF and NiCo<sub>2</sub>S<sub>4</sub> @NF.

#### 4. Conclusions

In summary, this paper directly synthesized the pure-phase doped electrocatalyst Fe-NiCo<sub>2</sub>S<sub>4</sub> @NIF on the NIF surface by the molten salt method and trojan strategy. Physical characterization reveals that the pure phase nanoparticles with pores have good mechanical strength. And DFT calculations suggest that doped Fe can promote charge transfer, enhance the conductivity of the electrocatalyst and lower the \*OOH energy barrier. Therefore, the prepared Fe-NiCo<sub>2</sub>S<sub>4</sub> @NIF exhibits superior OER performance with a lower overpotential of 325 mV to drive the industrial current density of 1000 mA cm<sup>-2</sup> and robust stability for 1000 h at 1000 mA cm<sup>-2</sup>. When this electrocatalyst (anode) is assembled with commercial Pt/C (cathode) as a single-cell AEM electrolyzer (Fe-NiCo<sub>2</sub>S<sub>4</sub> @NIF/(Pt/C)), which demonstrates remarkable performance (1000 mA cm<sup>-2</sup> at 1.83 V<sub>cell</sub>) and excellent energetic efficiency

(72% at 1000 mA cm<sup>-2</sup>) during a 100-h practical test. This work provides a simple and efficient strategy for the development of doped pure-phase OER electrocatalysts and contributes to the industrialization of AEM water electrolysis.

#### CRediT authorship contribution statement

**Fu-Li Wang:** Data curation, Writing – original draft, Formal analysis, Investigation, Writing – review & editing. **Yi-Wen Dong:** Writing – original draft, Conceptualization, Formal analysis, Writing – review & editing. **Cheng-Jie Yu:** Writing – review & editing, Formal analysis. **Bin Dong:** Formal analysis, Investigation, Resources, Writing – original draft, Funding acquisition, Project administration, Writing – review & editing. **Xin-Yu Zhang:** Writing – original draft, Methodology. **Ruo-Yao Fan:** Writing – original draft, Formal analysis. **Jing-Yi Xie:** Writing –



original draft, Writing – review & editing. **Ya-Nan Zhou**: Writing – review & editing, Formal analysis. **Yong-Ming Chai**: Funding acquisition, Conceptualization, Investigation, Resources, Formal analysis, Supervision, Writing – review & editing.

## Declaration of Competing Interest

The authors declare that they have no known competing financial interests or personal relationships that could have appeared to influence the work reported in this paper.

## Data Availability

Data will be made available on request.

## Acknowledgments

This work is financially supported by the National Natural Science Foundation of China (52174283 and 52274308), Innovation Fund Project for Graduate Student of China University of Petroleum (East China) and the Fundamental Research Funds for the Central Universities (No. 23CX04028A).

## Appendix A. Supporting information

Supplementary data associated with this article can be found in the online version at [doi:10.1016/j.apcatb.2023.122660](https://doi.org/10.1016/j.apcatb.2023.122660).

## References

- [1] H. Chen, X. Liang, Y. Liu, X. Ai, T. Asefa, X. Zou, Active site engineering in porous electrocatalysts, *Adv. Mater.* 32 (2020) 2002435, <https://doi.org/10.1002/adma.202002435>.
- [2] X. Zhang, C. Feng, B. Dong, C. Liu, Y. Chai, High-voltage-enabled stable cobalt species deposition on MnO<sub>2</sub> for water oxidation in acid, *Adv. Mater.* (2023) 2207066, <https://doi.org/10.1002/adma.202207066>.
- [3] H. Chen, L. Shi, X. Liang, L. Wang, T. Asefa, X. Zou, Optimization of active sites via crystal phase, composition and morphology for efficient low-iridium oxygen evolution catalysts, *Angew. Chem. Int. Ed.* 59 (2020) 19654–19658, <https://doi.org/10.1002/anie.202006756>.
- [4] B. Dong, Y.N. Zhou, J.C. Zhou, Y. Ma, N. Yu, R.N. Luan, Y.W. Dong, Y.M. Chai, Underpotential deposition promoting low Pt loading on MoO<sub>3</sub>/MoS<sub>2</sub> heterostructure towards efficient wide pH hydrogen evolution, *Fuel* 324 (2022), 124343, <https://doi.org/10.1016/j.fuel.2022.124343>.
- [5] J.Y. Zhang, Y. Yan, B. Mei, R. Qi, T. He, Z. Wang, W. Fang, S. Zaman, Y. Su, S. Ding, B.Y. Xia, Local spin-state tuning of cobalt-iron selenide nanoframes for the boosted oxygen evolution, *Energy Environ. Sci.* 14 (2021) 365–373, <https://doi.org/10.1039/D0EE03500A>.
- [6] Y. Huang, L.W. Jiang, X.L. Liu, T. Tan, H. Liu, J.J. Wang, Precisely engineering the electronic structure of active sites boosts the activity of iron-nickel selenide on nickel foam for highly efficient and stable overall water splitting, *Appl. Catal. B Environ.* 299 (2021), 120678, <https://doi.org/10.1016/j.apcatb.2021.120678>.
- [7] J. Li, Oxygen Evolution Reaction in energy conversion and storage: design strategies under and beyond the energy scaling relationship, *Nano-Micro Lett.* 14 (2022) 112, <https://doi.org/10.1007/s40820-022-00857-x>.
- [8] X.P. Li, C. Huang, W.K. Han, T. Ouyang, Z.Q. Liu, Transition metal-based electrocatalysts for overall water splitting, *Chin. Chem. Lett.* 32 (2021) 2597–2616, <https://doi.org/10.1016/j.ccl.2021.01.047>.
- [9] W. Yu, Z. Chen, Y. Fu, W. Xiao, T. Ma, B. Dong, Y. Chai, Z. Wu, L. Wang, Co-Mo microcolumns decorated with trace Pt for large current density hydrogen generation in alkaline seawater, *Appl. Catal. B Environ.* 317 (2022), 121762, <https://doi.org/10.1016/j.apcatb.2022.121762>.
- [10] J. Li, J. Li, J. Ren, H. Hong, D. Liu, L. Liu, D. Wang, Electric-field-treated Ni/Co<sub>3</sub>O<sub>4</sub> film as high-performance bifunctional electrocatalysts for efficient overall water splitting, *Nano-Micro Lett.* 14 (2022) 148, <https://doi.org/10.1007/s40820-022-00889-3>.
- [11] W. Zhang, Y. Tang, L. Yu, X.Y. Yu, Activating the alkaline hydrogen evolution performance of Mo-incorporated Ni(OH)<sub>2</sub> by plasma-induced heterostructure, *Appl. Catal. B Environ.* 266 (2020), 118154, <https://doi.org/10.1016/j.apcatb.2019.118154>.
- [12] H. Yang, L. Gong, H. Wang, C. Dong, J. Wang, K. Qi, H. Liu, X. Guo, B.Y. Xia, Preparation of nickel-iron hydroxides by microorganism corrosion for efficient oxygen evolution, *Nat. Commun.* 11 (2020) 5075, <https://doi.org/10.1038/s41467-020-18891-x>.
- [13] Y. Tang, Q. Liu, L. Dong, H.B. Wu, X.Y. Yu, Activating the hydrogen evolution and overall water splitting performance of NiFe LDH by cation doping and plasma reduction, *Appl. Catal. B Environ.* 266 (2020), 118627, <https://doi.org/10.1016/j.apcatb.2020.118627>.
- [14] R.Y. Fan, Y.N. Zhou, M.X. Li, J.Y. Xie, W.L. Yu, J.Q. Chi, L. Wang, J.F. Yu, Y. M. Chai, B. Dong, In situ construction of Fe(Co)OOH through ultra-fast electrochemical activation as real catalytic species for enhanced water oxidation, *Chem. Eng. J.* 426 (2021), 131943, <https://doi.org/10.1016/j.cej.2021.131943>.
- [15] S.J. Xu, Y.N. Zhou, G.P. Shen, B. Dong, Ni(OH)<sub>2</sub> derived from NiS<sub>2</sub> induced by reflux playing three roles for hydrogen/oxygen evolution reaction, *Chin. J. Struct. Chem.* 41 (2022) 2208052–2208057, <https://doi.org/10.14102/j.cnki.0254-5861.2022-0143>.
- [16] R.Y. Fan, J.Y. Xie, H.J. Liu, H.Y. Wang, M.X. Li, N. Yu, R.N. Luan, Y.M. Chai, B. Dong, Directional regulating dynamic equilibrium to continuously update electrocatalytic interface for oxygen evolution reaction, *Chem. Eng. J.* 431 (2022), 134040, <https://doi.org/10.1016/j.cej.2021.134040>.
- [17] J. Zhou, L. Yu, Q. Zhou, C. Huang, Y. Zhang, B. Yu, Y. Yu, Ultrafast fabrication of porous transition metal foams for efficient electrocatalytic water splitting, *Appl. Catal. B Environ.* 288 (2021), 120002, <https://doi.org/10.1016/j.apcatb.2021.120002>.
- [18] K. Yue, J. Liu, Y. Zhu, C. Xia, P. Wang, J. Zhang, Y. Kong, X. Wang, Y. Yan, B.Y. Xia, In situ ion-exchange preparation and topological transformation of trimetal-organic frameworks for efficient electrocatalytic water oxidation, *Energy Environ. Sci.* 14 (2021) 6546–6553, <https://doi.org/10.1039/D1EE02606B>.
- [19] C. Yan, J. Huang, C. Wu, Y. Li, Y. Tan, L. Zhang, Y. Sun, X. Huang, J. Xiong, In-situ formed NiS/Ni coupled interface for efficient oxygen evolution and hydrogen evolution, *J. Mater. Sci. Technol.* 42 (2020) 10–16, <https://doi.org/10.1016/j.jmst.2019.08.042>.
- [20] P. He, Y. Xie, Y. Dou, J. Zhou, A. Zhou, X. Wei, J.R. Li, Partial sulfurization of a 2D MOF array for highly efficient oxygen evolution reaction, *ACS Appl. Mater. Interfaces* 11 (2019) 41595–41601, <https://doi.org/10.1021/acsami.9b16224>.
- [21] Y.N. Zhou, W.L. Yu, Y.N. Cao, J. Zhao, B. Dong, Y. Ma, F.L. Wang, R.Y. Fan, Y. L. Zhou, Y.M. Chai, S-doped nickel-iron hydroxides synthesized by room-temperature electrochemical activation for efficient oxygen evolution, *Appl. Catal. B Environ.* 292 (2021), 120150, <https://doi.org/10.1016/j.apcatb.2021.120150>.
- [22] M. Zheng, K. Guo, W.J. Jiang, T. Tang, X. Wang, P. Zhou, J. Du, Y. Zhao, C. Xu, J. S. Hu, When MoS<sub>2</sub> meets FeOOH: a “one-stone-two-birds” heterostructure as a bifunctional electrocatalyst for efficient alkaline water splitting, *Appl. Catal. B Environ.* 244 (2019) 1004–1012, <https://doi.org/10.1016/j.apcatb.2018.12.019>.
- [23] P. Phonsuksawang, P. Khajondetchairit, T. Butburee, S. Sattayaporn, N. Chanlek, P. Hirunsit, S. Suthirakun, T. Siritanon, Effects of Fe doping on enhancing electrochemical properties of NiCo<sub>2</sub>S<sub>4</sub> supercapacitor electrode, *Electrochim. Acta* 340 (2020), 135939, <https://doi.org/10.1016/j.electacta.2020.135939>.
- [24] H. Liu, Q. He, H. Jiang, Y. Lin, Y. Zhang, M. Habib, S. Chen, L. Song, Electronic structure reconfiguration toward pyrite NiS<sub>2</sub> via engineered heteroatom defect boosting overall water splitting, *ACS Nano* 11 (2017) 11574–11583, <https://doi.org/10.1021/acsnano.7b06501>.
- [25] W. Li, H. Zhao, H. Li, R. Wang, Fe doped NiS nanosheet arrays grown on carbon fiber paper for a highly efficient electrocatalytic oxygen evolution reaction, *Nanoscale Adv.* 4 (2022) 1220–1226, <https://doi.org/10.1039/D2NA00004K>.
- [26] Q. Xu, H. Jiang, X. Duan, Z. Jiang, Y. Hu, S.W. Boettcher, W. Zhang, S. Guo, C. Li, Fluorination-enabled reconstruction of NiFe electrocatalysts for efficient water oxidation, *Nano Lett.* 21 (2021) 492–499, <https://doi.org/10.1021/acs.nanolett.0c03950>.
- [27] Y. Xu, W. Zhang, Y. Li, P. Lu, Z.S. Wu, A general bimetal-ion adsorption strategy to prepare nickel single atom catalysts anchored on graphene for efficient oxygen evolution reaction, *J. Energy Chem.* 43 (2020) 52–57, <https://doi.org/10.1016/j.jechem.2019.08.006>.
- [28] F.L. Wang, X.Y. Zhang, J.C. Zhou, Z.N. Shi, B. Dong, J.Y. Xie, Y.W. Dong, J.F. Yu, Y. M. Chai, Amorphous-crystalline FeNi<sub>2</sub>S<sub>4</sub>@NiFe-LDH nanograsses with molten salt as an industrially promising electrocatalyst for oxygen evolution, *Inorg. Chem. Front.* 9 (2022) 2068–2080, <https://doi.org/10.1039/D2QI00003B>.
- [29] X. Chen, M. Li, J. Hou, K. Lu, X. Yue, Y. Li, L. Chen, Z. Liu, X. Yang, Molten salt method synthesis of multivalent cobalt and oxygen vacancy modified nitrogen-doped MXene as highly efficient hydrogen and oxygen evolution reaction electrocatalysts, *J. Colloid Interface Sci.* 615 (2022) 831–839, <https://doi.org/10.1016/j.jcis.2022.02.010>.
- [30] A. Arun, L. Kumar, A. Chowdhury, Structure-property relations for a phase-pure, nanograined tetragonal zirconia ceramic stabilized with minimum CaO doping, *J. Am. Ceram. Soc.* 104 (2021) 3497–3507, <https://doi.org/10.1111/jace.17683>.
- [31] C. Tang, H.F. Wang, Q. Zhang, Multiscale principles to boost reactivity in gas-involving energy electrocatalysis, *Acc. Chem. Res.* 51 (2018) 881–889, <https://doi.org/10.1021/acs.accounts.7b00616>.
- [32] Z. Hu, X. Xiao, H. Jin, T. Li, M. Chen, Z. Liang, Z. Guo, J. Li, J. Wan, L. Huang, Y. Zhang, G. Feng, J. Zhou, Rapid mass production of two-dimensional metal oxides and hydroxides via the molten salts method, *Nat. Commun.* 8 (2017) 15630, <https://doi.org/10.1038/ncomms15630>.
- [33] Z.L. Zhao, Q. Wang, X. Huang, Q. Feng, S. Gu, Z. Zhang, H. Xu, L. Zeng, M. Gu, H. Li, Boosting the oxygen evolution reaction using defect-rich ultra-thin ruthenium oxide nanosheets in acidic media, *Energy Environ. Sci.* 13 (2020) 5143–5151, <https://doi.org/10.1039/D0EE01960G>.
- [34] J.J. Kaczur, H. Yang, Z. Liu, S.D. Sajjad, R.I. Masel, Carbon dioxide and water electrolysis using new alkaline stable anion membranes, *Front. Chem.* 6 (2018) 263, <https://doi.org/10.3389/fchem.2018.00263>.
- [35] P. Thangavel, M. Ha, S. Kumaraguru, A. Meena, A.N. Singh, A.M. Harzandi, K. S. Kim, Graphene-nanoplatelets-supported NiFe-MOF: high-efficiency and ultra-stable oxygen electrodes for sustained alkaline anion exchange membrane water

- electrolysis, *Energy Environ. Sci.* 13 (2020) 3447–3458, <https://doi.org/10.1039/D0EE00877J>.
- [36] J. Lee, H. Jung, Y.S. Park, S. Woo, N. Kwon, Y. Xing, S.H. Oh, S.M. Choi, J.W. Han, B. Lim, Corrosion-engineered bimetallic oxide electrode as anode for high-efficiency anion exchange membrane water electrolyzer, *Chem. Eng. J.* 420 (2021), 127670, <https://doi.org/10.1016/j.cej.2020.127670>.
- [37] J. Lee, H. Jung, Y.S. Park, S. Woo, J. Yang, M.J. Jang, J. Jeong, N. Kwon, B. Lim, J. W. Han, S.M. Choi, High-efficiency anion-exchange membrane water electrolyzer enabled by ternary layered double hydroxide anode, *Small* 17 (2021) 2100639, <https://doi.org/10.1002/smll.202100639>.
- [38] O. Knop, K.I.G. Reid, Y. Nakagawa, S. Sutarno, Chalkogenides of the transition elements. VI. X-Ray, neutron, and magnetic investigation of the spinels  $\text{Co}_3\text{O}_4$ ,  $\text{NiCo}_2\text{O}_4$ ,  $\text{Co}_3\text{S}_4$ , and  $\text{NiCo}_2\text{S}_4$ , *Can. J. Chem.* 46 (1968) 3463–3476, <https://doi.org/10.1139/v68-576>.
- [39] F.L. Wang, X.Y. Li, Y.W. Dong, J. Nan, Y.M. Sun, H.B. Yu, X.Y. Zhang, B. Dong, Y. M. Chai, Strong ion interaction inducing ultrahigh activity of  $\text{NiCoP}$  nanowires for overall water splitting at large current density, *Appl. Surf. Sci.* 589 (2022), 152837, <https://doi.org/10.1016/j.apsusc.2022.152837>.
- [40] X. Wu, Y. Yang, T. Zhang, B. Wang, H. Xu, X. Yan, Y. Tang,  $\text{CeO}_x$ -decorated hierarchical  $\text{NiCo}_2\text{S}_4$  hollow nanotubes arrays for enhanced oxygen evolution reaction electrocatalysis, *ACS Appl. Mater. Interfaces* 11 (2019) 39841–39847, <https://doi.org/10.1021/acsami.9b12221>.
- [41] X. Zhang, Y. Qiu, Q. Li, X. Ji, J. Liu, Fe-atom-implantation induced regional phase reconstruction for high-entropy  $\text{Ni}_x\text{S}_y$  construction with diversified crystallographic orientations towards accelerated water splitting, *J. Power Sources* 522 (2022), 231004, <https://doi.org/10.1016/j.jpowsour.2022.231004>.
- [42] H. Su, S. Song, Y. Gao, N. Li, Y. Fu, L. Ge, W. Song, J. Liu, T. Ma, In situ electronic redistribution tuning of  $\text{NiCo}_2\text{S}_4$  nanosheets for enhanced electrocatalysis, *Adv. Funct. Mater.* 32 (2022) 2109731, <https://doi.org/10.1002/adfm.202109731>.
- [43] X.Y. Zhang, F.T. Li, Y.W. Dong, B. Dong, F.N. Dai, C.G. Liu, Y.M. Chai, Dynamic anion regulation to construct S-doped  $\text{FeOOH}$  realizing 1000  $\text{mA cm}^{-2}$ -level-current-density oxygen evolution over 1000h, *Appl. Catal. B Environ.* 315 (2022), 121571, <https://doi.org/10.1016/j.apcatb.2022.121571>.
- [44] M.X. Li, Y.N. Zhou, Y.W. Dong, X. Liu, R.N. Luan, B. Liu, J.B. Zeng, Y.M. Chai, B. Dong, Metal-rich heterostructure of Ag-doped  $\text{FeS}/\text{Fe}_2\text{P}$  for robust hydrogen evolution, *Int. J. Hydrog. Energy* 47 (2022) 20518–20528, <https://doi.org/10.1016/j.ijhydene.2022.04.166>.
- [45] H. Xu, J. Cao, C. Shan, B. Wang, P. Xi, W. Liu, Y. Tang, MOF-derived hollow  $\text{CoS}$  decorated with  $\text{CeO}_x$  nanoparticles for boosting oxygen evolution reaction electrocatalysis, *Angew. Chem. Int. Ed.* 57 (2018) 8654–8658, <https://doi.org/10.1002/anie.201804673>.
- [46] F. Lai, J. Feng, T. Heil, Z. Tian, J. Schmidt, G.C. Wang, M. Oschatz, Partially delocalized charge in Fe-doped  $\text{NiCo}_2\text{S}_4$  nanosheet-mesoporous carbon-composites for high-voltage supercapacitors, *J. Mater. Chem. A* 7 (2019) 19342–19347, <https://doi.org/10.1039/C9TA06250E>.
- [47] J. Hu, S. Li, J. Chu, S. Niu, J. Wang, Y. Du, Z. Li, X. Han, P. Xu, Understanding the phase-induced electrocatalytic oxygen evolution reaction activity on  $\text{FeOOH}$  nanostructures, *ACS Catal.* 9 (2019) 10705–10711, <https://doi.org/10.1021/acscatal.9b03876>.
- [48] K. Zhu, F. Shi, X. Zhu, W. Yang, The roles of oxygen vacancies in electrocatalytic oxygen evolution reaction, *Nano Energy* 73 (2020), 104761, <https://doi.org/10.1016/j.nanoen.2020.104761>.
- [49] X. Gong, S. Li, P.S. Lee, A fiber asymmetric supercapacitor based on  $\text{FeOOH}/\text{PPy}$  on carbon fibers as an anode electrode with high volumetric energy density for wearable applications, *Nanoscale* 9 (2017) 10794–10801, <https://doi.org/10.1039/C7NR02896B>.
- [50] Y. Liu, Y. Bai, W. Yang, J. Ma, K. Sun, Self-supported electrode of  $\text{NiCo-LDH}/\text{NiCo}_2\text{S}_4/\text{CC}$  with enhanced performance for oxygen evolution reaction and hydrogen evolution reaction, *Electrochim. Acta* 367 (2021), 137534, <https://doi.org/10.1016/j.electacta.2020.137534>.
- [51] X. Wang, W. Ma, Z. Xu, H. Wang, W. Fan, X. Zong, C. Li, Metal phosphide catalysts anchored on metal-caged graphitic carbon towards efficient and durable hydrogen evolution electrocatalysis, *Nano Energy* 48 (2018) 500–509, <https://doi.org/10.1016/j.nanoen.2018.04.011>.
- [52] C. Kuai, C. Xi, A. Hu, Y. Zhang, Z. Xu, D. Nordlund, C.J. Sun, C.A. Cadigan, R. M. Richards, L. Li, C.K. Dong, X.W. Du, F. Lin, Revealing the dynamics and roles of iron incorporation in nickel hydroxide water oxidation catalysts, *J. Am. Chem. Soc.* 143 (2021) 18519–18526, <https://doi.org/10.1021/jacs.1c07975>.
- [53] L. Trotochaud, S.L. Young, J.K. Ranney, S.W. Boettcher, Nickel-iron oxyhydroxide oxygen-evolution electrocatalysts: the role of intentional and incidental iron incorporation, *J. Am. Chem. Soc.* 136 (2014) 6744–6753, <https://doi.org/10.1021/ja502379c>.
- [54] M. Görlin, J. Ferreira de Araújo, H. Schmies, D. Bernsmeier, S. Dresp, M. Glicch, Z. Jusys, P. Cherev, R. Kraehnert, H. Dau, P. Strasser, Tracking catalyst redox states and reaction dynamics in Ni-Fe oxyhydroxide oxygen evolution reaction electrocatalysts: the role of catalyst support and electrolyte pH, *J. Am. Chem. Soc.* 139 (2017) 2070–2082, <https://doi.org/10.1021/jacs.6b12250>.
- [55] D. Zhao, K. Jiang, Y. Pi, X. Huang, Superior electrochemical oxygen evolution enabled by three-dimensional layered double hydroxide nanosheet superstructures, *ChemCatChem* 9 (2017) 84–88, <https://doi.org/10.1002/cctc.201601106>.
- [56] M.Y. Gao, J.R. Zeng, Q.B. Zhang, C. Yang, X.T. Li, Y.X. Hua, C.Y. Xu, Scalable one-step electrochemical deposition of nanoporous amorphous S-doped  $\text{NiFe}_2\text{O}_4/\text{Ni}_3\text{Fe}$  composite films as highly efficient electrocatalysts for oxygen evolution with ultrahigh stability, *J. Mater. Chem. A* 6 (2018) 1551–1560, <https://doi.org/10.1039/C7TA08474A>.
- [57] D. Xu, M.B. Stevens, M.R. Cosby, S.Z. Oener, A.M. Smith, L.J. Enman, K.E. Ayers, C. B. Capuano, J.N. Renner, N. Danilovic, Y. Li, H. Wang, Q. Zhang, S.W. Boettcher, Earth-abundant oxygen electrocatalysts for alkaline anion-exchange-membrane water electrolysis: effects of catalyst conductivity and comparison with performance in three-electrode cells, *ACS Catal.* 9 (2019) 7–15, <https://doi.org/10.1021/acscatal.8b04001>.
- [58] Q. Wen, K. Yang, D. Huang, G. Cheng, X. Ai, Y. Liu, J. Fang, H. Li, L. Yu, T. Zhai, Schottky heterojunction nanosheet array achieving high-current-density oxygen evolution for industrial water splitting electrolyzers, *Adv. Energy Mater.* 11 (2021) 2102353, <https://doi.org/10.1002/aenm.202102353>.
- [59] J. Zhang, X. Shang, H. Ren, J. Chi, H. Fu, B. Dong, C. Liu, Y. Chai, Modulation of inverse spinel  $\text{Fe}_3\text{O}_4$  by phosphorus doping as an industrially promising electrocatalyst for hydrogen evolution, *Adv. Mater.* 31 (2019) 1905107, <https://doi.org/10.1002/adma.201905107>.
- [60] X.Y. Zhang, F.L. Wang, J.Y. Fu, Y.N. Zhen, B. Dong, Y.N. Zhou, H.J. Liu, D.P. Liu, C. G. Liu, Y.M. Chai, Amorphous-crystalline catalytic interface of  $\text{CoFeOH}/\text{CoFeP}$  with double sites based on ultrafast hydrolysis for hydrogen evolution at high current density, *J. Power Sources* 507 (2021), 230279, <https://doi.org/10.1016/j.jpowsour.2021.230279>.
- [61] B. Konkena, J. Masa, A.J.R. Botz, I. Sinev, W. Xia, J. Kößmann, R. Drautz, M. Muhler, W. Schuhmann, Metallic  $\text{NiP}_3/\text{NiOOH}$  core-shell heterostructures as highly efficient and stable electrocatalyst for the oxygen evolution reaction, *ACS Catal.* 7 (2017) 229–237, <https://doi.org/10.1021/acscatal.6b02203>.
- [62] P. Phonsuksawang, P. Khajondetchairit, T. Butburee, S. Sattayaporn, N. Chanlek, P. Hirunsit, S. Suthirakun, T. Siritanon, Effects of Fe doping on enhancing electrochemical properties of  $\text{NiCo}_2\text{S}_4$  supercapacitor electrode, *Electrochim. Acta* 340 (2020), 135939, <https://doi.org/10.1016/j.electacta.2020.135939>.
- [63] S. Sun, X. Zhou, B. Cong, W. Hong, G. Chen, Tailoring the d-band centers endows  $(\text{Ni}_x\text{Fe}_{1-x})_2\text{P}$  nanosheets with efficient oxygen evolution catalysis, *ACS Catal.* 10 (2020) 9086–9097, <https://doi.org/10.1021/acscatal.0c01273>.